Los Alamos NATIONAL LABORATORY EST.1943

LA-UR-17-24487 (Accepted Manuscript)

In-Situ through-Plane Measurements of Ionic Potential Distributions in Non-Precious Metal Catalyst Electrode for PEFC

Komini Babu, Siddharth
Chung, Hoon Taek
Zelenay, Piotr
Litster, Shawn

Provided by the author(s) and the Los Alamos National Laboratory (2017-09-13).

To be published in: ECS Transactions

DOI to publisher's version: 10.1149/06917.0023ecst

Permalink to record: http://permalink.lanl.gov/object/view?what=info:lanl-repo/lareport/LA-UR-17-24487

Disclaimer:
Approved for public release. Los Alamos National Laboratory, an affirmative action/equal opportunity employer, is operated by the Los Alamos National Security, LLC for the National Nuclear Security Administration of the U.S. Department of Energy under contract DE-AC52-06NA25396. Los Alamos National Laboratory strongly supports academic freedom and a researcher's right to publish; as an institution, however, the Laboratory does not endorse the viewpoint of a publication or guarantee its technical correctness.

RESEARCH LIBRARY

In-Situ through-Plane Measurements of Ionic Potential Distributions in Non-Precious Metal Catalyst Electrode for PEFC

S. Komini Babu[a], H. T. Chung[b], P. Zelenay[b], and S. Litster[a]

[a] Department of Mechanical Engineering, Carnegie Mellon University, Pittsburgh, Pennsylvania 15217, USA
[b] Materials Physics and Applications, Los Alamos National Laboratory, Los Alamos, New Mexico 87545, USA

This manuscript presents micro-scale experimental diagnostics and nano-scale resolution X-ray imaging applied to the study of proton conduction in non-precious metal catalyst (NPMC) fuel cell cathodes. NPMC's have the potential to reduce the cost of the fuel cell for multiple applications. However, NPMC electrodes are inherently thick compared to the convention Pt/C electrode due to the lower volumetric activity. Thus, the electric potential drop through the Nafion across the electrode thickness can yield significant performance loss. Ionomer distributions in the NPMC electrodes with different ionomer loading are extracted from morphological data using nanoscale X-ray computed tomography (nano-XCT) imaging of the cathode. Microstructured electrode scaffold (MES) diagnostics are used to measure the electrolyte potential at discrete points across the thickness of the catalyst layer. Using that apparatus, the electrolyte potential drop, the through-thickness reaction distribution, and the proton conductivity are measured and correlated with the corresponding Nafion morphology and cell performance.

Introduction

Expensive platinum (Pt) or Pt alloys are typically used as oxygen reduction reaction (ORR) catalysts for the cathodes of acidic polymer electrolyte fuel cells (PEFC). The high Pt loading required in the cathode for satisfactory performance is an obstacle for commercialization due to the high raw material cost. Hence, there is significant interest in NPMC for cathodes. The activity and durability of ORR NPMC have significantly improved in the past decade (1–3). However, to generate current densities comparable to conventional Pt cathodes, the lower volumetric activity requires the NPMC cathodes to be an order of magnitude thicker. Increasing the electrode thickness increases the proton and oxygen transport resistance as well as making the electrode more susceptible to liquid water flooding. Therefore, understanding the relationships between the cathode architecture and performance is crucial for optimizing the performance of thick-format NPMC cathodes.

The ionomer distribution in the electrode influences ionic conductivity and thereby affects the fuel cell performance. The most common method of studying the ionomer distribution is by employing transmission electron microscopy (TEM) and Energy-dispersive X-ray spectroscopy (EDS). Recently it has been demonstrated that advanced TEM can directly map the ionomer from the TEM (4), although with a small

2D field of view. Lopez-Haro et al. (5) also used electron tomography with cesium ion (Cs^+) staining to image Nafion distribution as deposited on dispersed carbon supports (rather than in electrodes).

Here we present a comprehensive study of the ionomer distribution and corresponding effectiveness of the ionomer's proton transport during operation. The Nafion distribution in the cathode morphology is investigated for three different Nafion loadings. Similar to Lopez-Haro et al., here we have stained the Nafion with Cs^+ ions. The staining ion-exchanges the proton at the Nafion's sulfonic acid side sites with a higher atomic number Cs^+ ion, giving Nafion a higher X-ray absorption contrast relative to the carbon catalyst.

Due to the extreme thickness of the NPMC cathodes, existing in-situ techniques (e.g., electrochemical impedance spectroscopy) cannot be used to measure the conductivity during operation due to large non-uniformities in properties and reaction rates. In-situ ionic conductivity and through-plane potential distribution are measured using microelectrode scaffold (MES) diagnostic as previously developed in our group for a Pt electrode (6). MES consists of a cylindrical working electrode (cathode), a counter electrode (anode) and an electrolyte layer as shown in Figure 1. Eight different discrete sensing layers with H_2 reference electrodes are placed through the thickness of the cathode at its perimeter, enabling spatiotemporal measurement of the Nafion potential as a function of the distance from the membrane. Spatially, the slope and the rate of slope change provides us with a measure of the ORR distribution across the electrode. Ionic conductivity is additionally measured using a four wire resistance measurement technique (7). The potential drop across the sense layer is measured while applying a small perturbation current to the reference electrode for H_2 pumping to the anode. MES can potential be used to validate the model previously developed by our group (8).

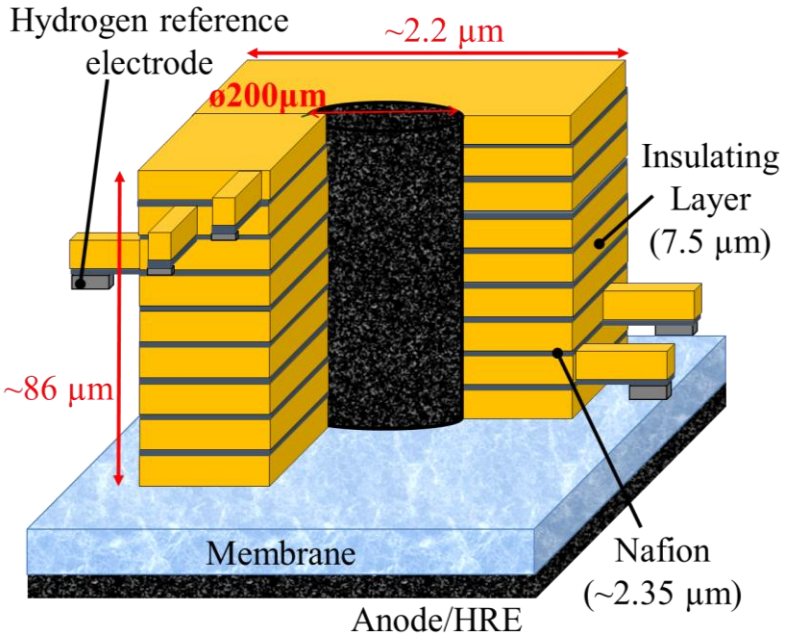

Figure 1. Schematic of an MES with eight alternating layers of insulating Kapton and Nafion film. Each sense layer has protruding tab with H_2 reference electrodes enabling in-situ measurement of the Nafion potential.

Experimental

NPMC powder and cathode

The present work employs a previously reported cyanamide-polyaniline-iron (CM-PANI-Fe) as the ORR catalyst (8). Briefly, a high surface area catalyst powder was prepared by high-temperature treatment followed by acid leaching of cyanamide, polyaniline and iron acetate precursors. The catalyst ink for the nano-CT imaged catalyst coated membranes (CCM) and the MES measurements was prepared by mixing and ultrasonicating the catalyst powder with a Nafion ionomer solution, deionized water, and isopropyl alcohol (IPA). The conventional CCMs were fabricated by painting the catalyst ink onto Nafion 211 membranes.

Nafion Imaging Using Nano-XCT

The sample to be imaged was prepared by cutting a small section of the CCM using a microscopy grade razor blade. The membrane side of the sample was epoxied onto a flat surface of a metal pin. The sample was milled using a micro-laser mill (Quiklaze 50ST2, New-Wave, Fremont, CA) such that the milled out slender pillar of catalyst layer remains completely inside the 65 µm x 65 µm field of view (FOV) of the nano-XCT. The samples were stained in a saturated solution of cesium sulfate (Sigma-Aldrich, St. Louis, MO) for 78 hrs. Small gold fiducials are placed at the top of the samples to correct minor sample drift during imaging when reconstructing the 3D CT image.

The morphological characteristic of the stained sample were imaged in 3D using a lab scale nano-XCT (UltraXRM-L200, Xradia Inc., Pleasanton, CA). Using its Zernike phase contrast mode (9), the catalyst layer was imaged to distinguish the solid (catalyst, Nafion) and the pore volumes. The same sample was also subsequently imaged by absorption contrast mode to distinguish the Cs^+ stained Nafion film. Both the modes of contrast imaging were done at large field of view (LFOV) imaging mode (150 nm resolution; 65 µm FOV). A total of 901 projection angles were used. The reconstructed data was analyzed using Avizo Fire (FEI Visualization Sciences Group, Burlington, MA) and custom MATLAB (Mathworks, Natick, MA) codes.

MES Experiments

Fabrication. The MES is based on a substrate of alternating Nafion sense layers and Kapton insulating layers. The Nafion sense films were fabricated by spin coating 15 wt. % Nafion solution, prepared by diluting 20 wt. % Nafion solution (D2020, IonPower, New Castle, DE) with deionized water and IPA, on a 7.5 µm thick Kapton film. The Nafion-coated Kapton films were cut into the desired shape, i.e., square shape with a protruding tab for contact with a hydrogen reference electrode (HRE). Eight sense films were stacked such the each protruding tab was aligned to a HRE in the fuel cell hardware as shown in Figure 1. The stack was hot-pressed, with the addition of an un-coated Kapton film for ionic isolation from the membrane, at 50 psi and 125ºC for 8 min. The thickness of the hot pressed films was 86.3 µm, consistent with a Nafion film thickness of approximately 2 µm. A 200 µm diameter through hole was cut at the center of the stack using the laser mill. Nafion 115 membrane was cut to match the square of the stack and

hot pressed together with the same condition as the before. The catalyst ink was hand painted into the hole until it was filled. Commercial gas diffusion electrodes (GDE) were used for the anode and the HREs, while a commercial gas diffusion layer (GDL) (SGL 24BC, IonPower, New Castle, DE) was used on the cathode side.

Hardware. The custom fuel cell hardware used for the MES experiments was described previously by An et al. (7). In brief, the anode flow field plate was modified to position eight reference electrodes around the anode. Printed circuit board in contact with the anode and the reference electrodes act as the anode current collector. A fuel cell test stand (FCT-150, Biologic, France) was used to control the flow rate and humidity of the gases. The fuel cell voltage and the current were controlled and measured respectively by a potentiostat (SP-150, BIO-logic, Knoxville, TN). The potential at the sense layers were measured using a data acquisition system (National Instruments, Austin, TX).

Polarization Curve. The MES polarization curves were obtained galvanostatically. Each potential were applied for 60 seconds for greater than 0.7 V in steps of 0.02 V. For lower than 0.7V, the potential was applied for 10 minutes in steps of 0.1 V. Last 20% of the measured current in each step was averaged.

Potential Measurement. The electrolyte potential was measured using the HREs connected to the MES sense layers. A data acquisition system was used to simultaneously record the potentials at sense layers located at the different discrete location through the thickness of the electrode as shown in Figure 2a. Fuel cell potential was applied in steps using a potentiostat. Each potential was held for 10 s.

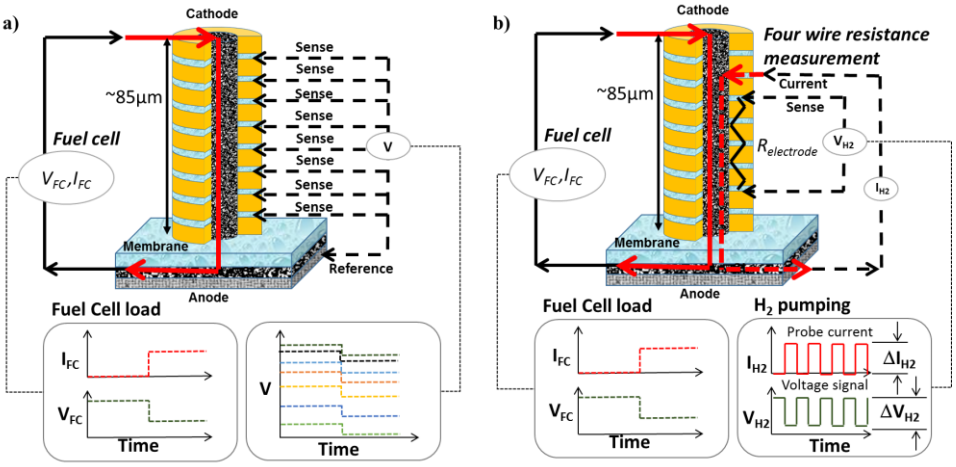

Figure 2.Schematic of the spatiotemporal measurement using MES. a) Ionic potential measurement at different locations through the thickness of the electrode. b) In-situ conductivity measurement using four wire measurement technique.

Conductivity Measurement. The ionic conductivity of an operating electrode was measured during the fuel cell operation by a modified four wire measurement technique. A potentiostat was used to apply a potential and record the corresponding fuel cell current. A second potentiostat applied a small DC perturbation H_2 pumping current between the anode and a reference electrode attached to a sense layer close to the GDL (7^{th} electrode from the membrane) (see Figure 2b). The perturbation current was small as to not affect the fuel cell operation. The corresponding potential drop was measured between the 2^{nd}

and 6th sense layer from the membrane. The resistance of the catalyst layer was calculated by:

$$R = \frac{\Delta V_{H_2}}{\Delta I_{H_2}} \quad [1]$$

where ΔI_{H_2} is the applied perturbation current and ΔV_{H_2} is the measured potential drop. Similarly the conductivity was calculated using:

$$\sigma = \frac{L}{RA} \quad [2]$$

where *A* is the electrode area and *L* is the center to center distance between the 2nd and 6th sense layer from the membrane.

Result and discussion

Nano-XCT imaging

We now discuss our results using nano-XCT to image the Nafion distribution in NPMC cathodes using a combination of Zernike phase contrast for the solid/pore structure and X-ray absorption contrast that resolves the Cs+ stained Nafion. The NPMC cathode studied here were previously shown by nano-XCT to have large macropores (>500 nm) with dense catalyst agglomerates on the order of several micrometers (8). The large dense agglomerates of comprised of smaller pores with length scales 100-500 nm. Figures 3a and 3b show reconstructed virtual slices from a plane across a pillar of the electrode in both absorption and Zernike phase contrast for CM-PANI-Fe with 50 wt. % Nafion loading. As Figure 3b shows, the Zernike phase contrast can distinguish the pore from the solid, but cannot distinguish the Nafion. In comparison, the absorption contrast image in Figure 3a shows the Nafion distribution but does not convey the electrode structure evident in the phase contrast image. Combining the data from phase and absorption contrast enables the distinction of the three domains: the pore, the catalyst, and the Nafion (10).

To enable comparison with different samples, the reconstructed images were normalized using the gold fiducial and air intensities. In absorption contrast imaging, the normalization is essential for a quantitative comparison of the samples with different Nafion loading. Figure 4a, 4b, and 4c shows the virtual normalized slices of NPMC with 35, 50, and 60 wt. % Nafion loading respectively in absorption contrast mode. The color intensity in the image is proportional to the local density of Nafion. The sample with 35 wt. % Nafion shows that the Nafion is distributed sparsely and is agglomerated outside of the catalyst agglomerates. Another NPMC sample with 35wt. % Nafion loading was prepared and imaged to confirm the distinct agglomeration of Nafion at this loading as well as the lack of Nafion intrusion into the catalyst. In comparison to 35 wt. %, 50 and 60 wt. % Nafion loading shows good intrusion into the micropores as shown in Figure 4b and 4c. In the 60 wt. % Nafion loading, intrusion into the micropores is similar to the 50 wt. % with the additional Nafion forming thick films around the catalyst agglomerates. In Figure 4c, the thickness of the Nafion film around the dense agglomerates is in the order of a few hundred nm. Figure 4c, 4d, and 4e shows the 3D reconstruction of the

Nafion distribution in CM-PANI-Fe 35 wt. %, 50 wt. % and 60wt. % Nafion loading respectively.

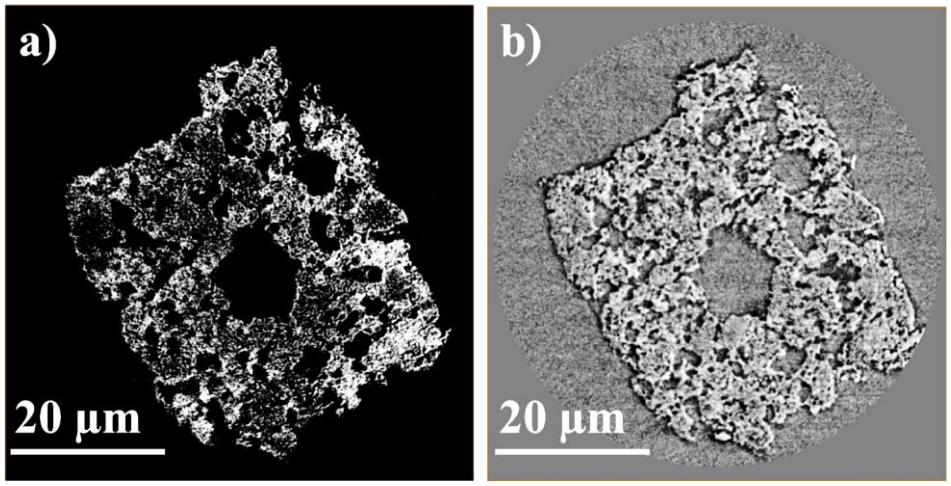

Figure 3. Nano-XCT imaging of CM-PANI-Fe 50 wt. % Nafion loading. Virtual slices in a) absorption and b) Zernike phase contrast. Nafion domain from absorption contrast was used to separate the catalyst domain from the solid domain in phase contrast.

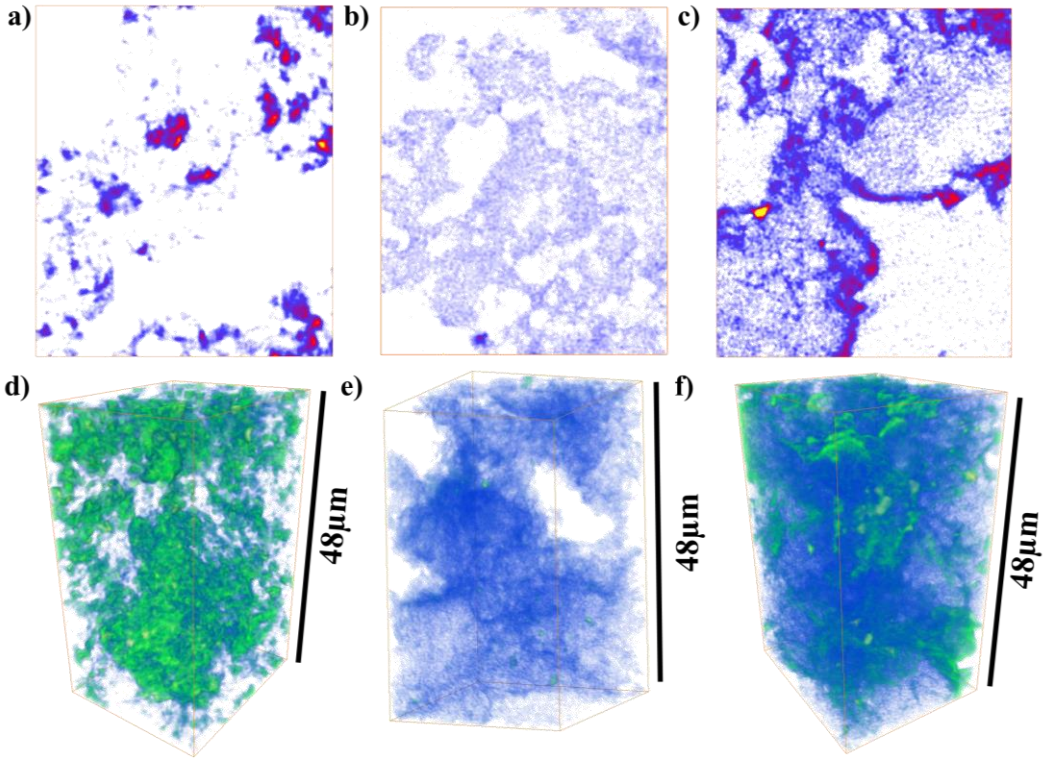

Figure 4. Virtual slices of the absorption contrast. NPMC catalyst with a) 35 wt. % b) 50 wt. % and c) 60 wt. % Nafion loading. The intensity of color in the slices shows the local density of Nafion. 3D volume renderings of Nafion for d) 35 wt. %, e) 50 wt. %, and f) 60 wt. % Nafion loadings.

NPMC cathode CCMs with the same Nafion loadings were also electrochemical tested for fuel cell performance while operating on 1 atm air at 80^{o}C. The performance of

those CCMs were previously reported (11) and Figure 5 shows the polarization curves for the different Nafion loadings all with the same catalyst loading. There is a good correspondence between the differences in performance and the corresponding Nafion distribution images in Figure 4. The low 35 wt. % polarization curve shows higher activation losses at low currents for the same amount of catalyst, which is consistent with the poor intrusion of Nafion into the catalyst. Likewise, we see significantly larger flooding mass transport losses with 60 % wt. Nafion loading, which is likely a result of the increased wetting of the macropores with a thick Nafion coating.

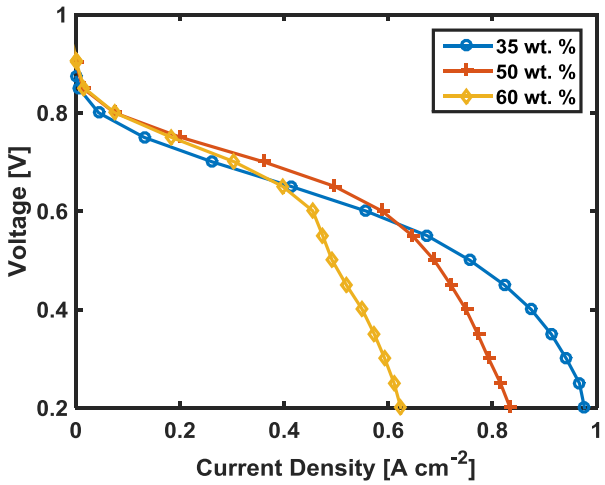

Figure 5. Polarization curves for CCMs featuring NPMC cathodes with Nafion loadings of 35, 50, and 60 wt. % when operating on fully humidified air and hydrogen at 100% relative humidity and 1 atm with a cell temperature of 80°C (11). Anode loading was 2.0 mg_{Pt} cm^{-2}. Anode/cathode flow rates were 200/200 sccm respectively.

MES Experiments

We now present the results of using the MES experimental apparatus to study the through-plane reaction distribution in a thick NPMC cathode. Key areas of interest are sensitivity of the reaction to hydration. It is often observed that with thick NPMC cathodes, the mass transport regime often features steep linear polarizations, similar to a large Ohmic loss. Such a feature is observed in the 60 % wt. curve in Figure 5, where the mass transport loss resembles a significantly increased Ohmic loss at higher currents rather than the typical shape observed at 35 % wt. We use the MES experiments to investigate the origin of this polarization curve feature. We also use the MES apparatus to measure the electrode's electrolyte conductivity during operation with internal water generation.

Polarization Curve. Figure 6 shows the polarization for the 50 wt. % Nafion loading sample at 50%, 80 %, and 140% RH in the cathode. The 140% RH is based on dew point and ensures fully saturated gases. During all the tests, the anode was maintained at 80% RH. Due to the small diameter of the MES hole's area compared to the Nafion membrane's area, the water activity in the membrane and at the cathode/membrane interface will be largely dominated by the 80% RH of the anode gas stream. Thus, the activation region and the initial Ohmic region of the curves do not show a significant variation due to changes in the cathode's air RH. However, the mass transfer

regions show a large variation in the performance due to the restricted water removal through the Nafion membrane and accumulation of liquid water in the cathode at higher RH and currents. The 50% RH curve is dominated by activation and Ohmic losses and no apparent mass transport loss. At 80% RH, there is slight reduced Ohmic loss, but also the onset of some mass transport loss. At 140% RH, the second Ohmic slope described above is observed.

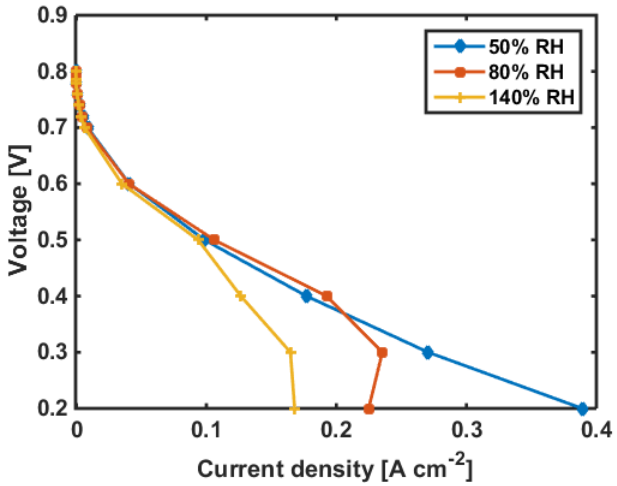

Figure 6. Polarization curves for CM-PANI-Fe 50 wt. % Nafion loading using the MES. Anode Pt loading was 0.35 mg_{Pt} cm^{-2} at three cathode RH levels. Anode RH was 80%. The anode/cathode gas flow rates were 200/200 sccm.

Nafion Potential Distribution. Figure 7a shows the time vs. measured potential at each of the sense layers. The potential measured at the sense layer reference electrodes are with respect to the fuel cell anode as shown in Figure 7b. It can be seen from the time series that the magnitude of the potential difference between the sense layers increases with decreases in fuel cell voltage because the higher currents yielded higher Ohmic drop across the electrode. The primary reason for the potential difference between two sense layers is due the ohmic drop within that section of the sense layers. Thus, the greater the difference in potentials between adjacent sense layers, the larger the local proton current through the electrode. Decreases in the potential difference moving from the membrane to the GDL is consistent with reducing proton current as the protons are consumed by the ORR.

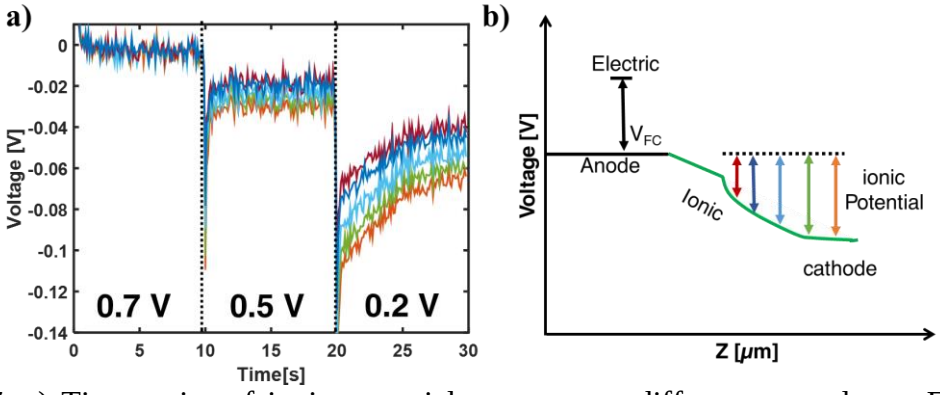

Figure 7. a) Time series of ionic potential measures at different sense layer. Fuel cell potential is held at 0.7 V, 0.5V, and 0.2V for 10 seconds. b) Schematic of the measured ionic potential at sense layer with respect to the fuel cell anode voltage.

The plot of the potential drop vs. the thickness of the electrode was obtained by averaging the last 25% of the potential drop in time series for each sense layer. Figure 8 shows potential distribution normalized by current density across the electrode at 0.2V. The curves are normalized so the shape of the curve can be better compared since the different currents obtained at the same potential caused shifts in the raw potential at the different RH levels of 50, 80, and 140%. The potential curves in certain cases exhibit a linear profile while a non-linear curve in other instances. At 50 % RH, we observe the distribution is flat in the last 30 µm next to GDL, consistent with little ORR because Ohmic losses concentrate the ORR near the membrane. The more linear potential distribution at high RH is due to the ORR reaction shifting towards the location near the MPL due to either oxygen transport resistance or flooding in the catalyst layer. In the case of flooding, a considerable portion of the cathode catalyst layer away from the MPL acts like a membrane with poor conductivity causing a huge ohmic resistance. Thus, the origin of the second Ohmic slope is the complete flooding of the cathode making it largely inactive except for a thin region adjacent to GDL.

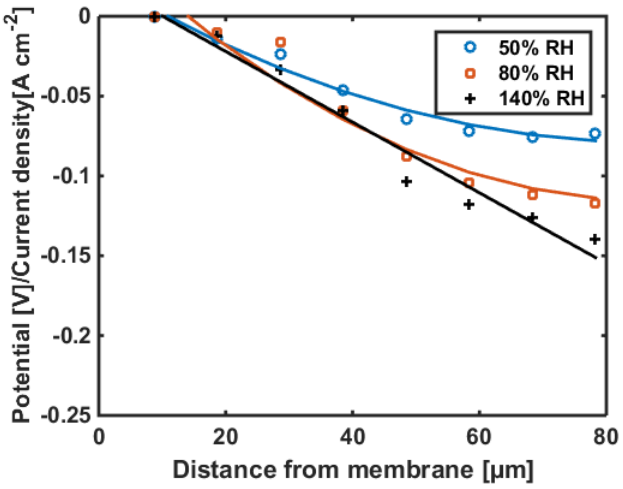

Figure 8. Current density normalized electrolyte potential distribution through the thickness of the electrode for CM-PANI-Fe 50 wt. % Nafion loading.

Ionic Conductivity. Figure 9 shows the in-situ in-operando measured catalyst layer conductivity using the modified four wire resistance measurement technique. Figure 9a shows conductivity increases with increase in RH at open circuit voltage (OCV). During the fuel cell operation at 50% and 80% RH, ionic conductivity plotted in Figure 9b is consistently around 0.6 S/m at all fuel cell potentials. This likely because of the large water reservoir in the adjacent membrane with fixed water activity matching the 80% in the anode. In the case of 140% RH, the conductivity increases with increased in current density at lower potential. This suggests significant uptake of water generated by the ORR increases the proton conductivity in the catalyst layer. This is also supported by the fact that conductivity is notably higher during operation than at equilibrium in the OCV condition without water generation.

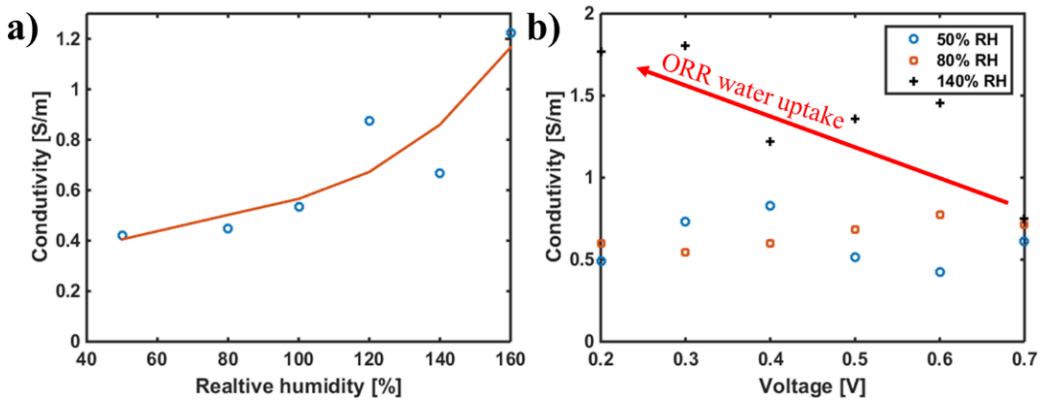

Figure 9. The Ionic conductivity of CM-PANI-Fe 50wt. % Nafion loading electrode. a) Effect of the RH on conductivity at OCV. b) Conductivity as a function of both RH and fuel cell operating voltages. The anode RH was 80 % in all cases.

Conclusion

This paper presents a novel in-situ experimentation and nano-XCT imaging to investigate the proton conduction in thick NPMC electrodes. We characterize the morphological distribution of Nafion binder in the catalyst using nano-XCT. The catalyst layers are stained with cesium sulfate to ion-exchange the proton in the Nafion binder with Cs^+ ions to increase the contrast of Nafion film while imaging. We found that the large activation losses at 35 % wt. Nafion loading were due low intrusion of Nafion into the catalyst, whereas significant flooding with 60 % wt. can be attributed to thick Nafion films in the large pores. Using the MES experimental setup, the ionic potential is measured at discrete points through the thickness of the electrodes to infer the ORR current density distribution across the electrode. We observe the ORR focused near the membrane in drier conditions, while at high RH the ORR is highly concentrated at GDL interface. The proton conductivity measurements show that conductivity is quite sensitive to RH as well as the rate of ORR water generation.

Acknowledgments

The authors gratefully acknowledge the support the support of the technology development manager Nancy Garland and funding from the US Department of Energy, the Office of Energy Efficiency and Renewable Energy, Office of Fuel Cell Technologies. The nano-XCT instrument was acquired with the support of a Major Research Infrastructure award from the National Science Foundation under Grant No. 1229090.

References

1. H. T. Chung, J. H. Won, and P. Zelenay, *Nat. Commun.*, **4**, 1922 (2013).
2. D. C. Higgins and Z. Chen, *Can. J. Chem. Eng.*, **91**, 1881–1895 (2013).
3. F. Jaouen et al., *Energy Environ. Sci.*, **4**, 114 (2011).
4. K. More, *2015 Annu. Merit Rev. Proc.* (2015).
5. M. Lopez-Haro, L. Guétaz, T. Printemps, A. Morin, S. Escribano, P-H. Jouneau, P. Bayle-Guillemaud, F. Chandezon, G. Gebel, *Nat. Commun.*, **5**, 5229 (2014).

6. K. C. Hess, W. K. Epting, and S. Litster, *Anal. Chem.*, **83**, 9492–8 (2011).
7. S. J. An and S. Litster, *ECS Trans.*, **58**, 831–839 (2013).
8. S. Komini Babu, H. T. Chung, G. Wu, P. Zelenay, and S. Litster, *ECS Trans.*, **64**, 281–292 (2014).
9. W. K. Epting, J. Gelb, and S. Litster, *Adv. Funct. Mater.*, **22**, 555–560 (2012).
10. S. Komini Babu, A. I. Mohamed, J. F. Whitacre, and S. Litster, *J. Power Sources*, **283**, 314–319 (2015).
11. P. Zelenay, *2014 Annu. Merit Rev. Proc.* (2014).